The periodic pulse photothermal radiometry technique within the front face configuration

Article *in* Measurement · March 2020

DOI: 10.1016/j.measurement.2020.107691

CITATIONS
10

READS
297

8 authors, including:

Jean-Luc Battaglia
University of Bordeaux
210 PUBLICATIONS **2,352** CITATIONS
SEE PROFILE

Emmanuel Ruffio
Institut de Mécanique et d'Ingénierie de Bordeaux
16 PUBLICATIONS **86** CITATIONS
SEE PROFILE

Andrzej Kusiak
University of Bordeaux
94 PUBLICATIONS **851** CITATIONS
SEE PROFILE

Christophe Pradere
Institut de Mécanique et d'Ingénierie de Bordeaux
148 PUBLICATIONS **1,570** CITATIONS
SEE PROFILE

The periodic pulse photothermal radiometry technique within the front face configuration

Jean-Luc Battaglia, Emmanuel Ruffio, Andrzej Kusiak, Christophe Pradere, Emmanuelle Abisset, Stéphane Chevalier, Alain Sommier, Jean-Christophe Batsale

I2M Lab., UMR CNRS 5295, University of Bordeaux, 351 cours de la libération, 33400 Talence

Abstract

The front face photothermal radiometry technique has been improved in order to estimate the thermal conductivity of thin films with better accuracy compared to existing techniques. The experimental procedure is based on the front face response to a nanoseconds laser pulse repeated periodically at high frequency, i. e., a Dirac comb waveform. Averaging the thermal response by considering thousands successive pulses allows improving largely the signal noise ratio. The unknown thermal properties and related experimental parameters are identified by minimizing the gap between the measured signal and the theoretical response that accounts with the pulse waveform, the repetition frequency and the detector transfer function. Minimization is first achieved by implementing first a simplex technique that gives an initial set of values to start the Metropolis-Hastings algorithm in a second step. Application of the proposed methodology is done considering amorphous GeTe film deposited on a Si wafer. It is shown that this experimental method as well as the implementation of the Bayes minimization technique allows to identify the thin film intrinsic thermal conductivity with high accuracy considering some uncertainty on the other parameters assumed to be known.

Keywords: thin films, thermal conductivity, interface thermal resistance, photothermal radiometry, Dirac comb excitation, Bayesian estimation.

1. Introduction

The thermal characterization of thin films and related thermal resistance at the interfaces with neighborhood materials is still a domain of continuous improvements. The investigated film is generally deposited on a substrate and

Email address: jean-luc.battaglia@u-bordeaux.fr (Jean-Luc Battaglia, Emmanuel Ruffio, Andrzej Kusiak, Christophe Pradere, Emmanuelle Abisset, Stéphane Chevalier, Alain Sommier, Jean-Christophe Batsale)

can be part also of a stack of other thin layers. This kind of multilayer sample is common in the fields of electronic devices, thermal protection within high temperature applications in aeronautics engines or machining tools for instance. Several kind of experimental procedures have been developed along time to measure the thermal properties of the films. They are all based on the thermal disturbance of the material, initially at uniform temperature, using a heat source that is classically a heat flux. Within the front face configuration, the heat flux is applied at the surface of the material, using generally a laser, and the relative change of temperature is monitored at the same location. When the heat source is generated as a pulse, mathematically described as a Dirac function, this experiment is so-called the front face flash technique. However, a periodic heat flux can be also implemented that leads monitoring the amplitude and the phase between the temperature and the source using a lock-in amplifier. Contact methods, as the 3ω technique [1, 2], have been extensively used since they offered absolute measurements of the heat flux and the temperature and they are also well suited with characterization at low temperature. At high temperature, the contactless photothermal methods, as the visible (VIS) thermoreflectance [3, 4, 5, 6, 7, 8] and the infrared (IR) radiometry techniques [9, 10, 11, 12, 13, 14], have been implemented and allow measuring relative change of the temperature and the heat flux. Within those experimental configurations, the calibration can be a complex task and it is highly advised to work with relative measurements, for both the heat flux and the temperature, instead of absolute ones. The classical requirement in such experiments is to generate very limited temperature increase at the surface (in practice < 10 K) in order to (i) ensure the linearity assumption that assumes the thermal properties of the material do not vary during the thermal disturbance (ii) assume the linear proportionality of the emitted radiation and the temperature at the surface. This latter is of particular interest when using a sensor in the IR, either a detector or a camera, to monitor the time-varying surface temperature at the heated area. Whatever the method used, the seek thermal properties are always deduced from the comparison of the measured data with the response of a model that is assumed to mimic the experimental configuration. This is the so-called inverse procedure that rests on a minimization process between theory and experiment [15, 16].

Within the field of the photothermal methods based on IR radiometry using the front face configuration, transient measurement are very sensitive to noise. Last developments based on modulated heat flux waveform show interesting results within MHz range [14]. However, since pulsed lasers offer wide possibilities of use in terms of power, pulse duration, implementation, wavelength and cost, it is proposed within the present paper to improve this measurement technique by heating the sample considering the heat flux waveform as a Dirac comb, i. e., generating low-energy nanoseconds heat pulses at a repetition frequency $1/T_r$. The temperature increase at the surface of the sample is therefore constituted as the sum of a DC and AC signals. Using low-energy pulses fulfills the requirement of low amplitude for both the continuous and transient contributions as explained previously. Once the continuous (DC) regime is stabilized, due to heat losses with the ambient, the transient (AC) response is recorded

considering N_s successive pulses, leading to N_s columns vectors $\overline{T_i}(t)_{i=1,N_s}$, $0 < t < T_r$, of the spatial average temperature at the aimed area by the detector. Assuming an accurate repeatability of the heat pulse at each period, differences between N_s recorded temperature vectors are only related to the measurement noise. By computing real-time averaging, the resulting vector $\left\langle \overline{T}(t) \right\rangle_n = \left[\overline{T_n}(t) + \sum_{i=1}^{n-1} \overline{T_i}(t) / (n-1) \right] /2$ for pulse n, with $1 \leq n \leq N_s$, shows an improved signal noise ratio. Assuming the N_s vectors are statistically independent, the noise standard deviation of temperature values $\left\langle \overline{T}(t) \right\rangle_{N_s}$ is theoretically reduced by $\sqrt{N_s}$ compared to $\overline{T_i}(t)_{i=1,N_s}$.

The experimental setup is presented is section 2. The heat transfer model related to the experimental configuration is described in section 3. Solution of the partial differential equations is achieved using Laplace and Hankel integral transforms and the quadrupole technique [17, 18, 19]. The periodic cumulative effect of the pulses is considered also that still leads to an analytical expression of the average surface temperature in space and time. A sensitivity analysis is performed in section 4 in order to optimize the experimental operating conditions. The identification procedure of the unknown parameters is also presented in this section. It is based on the use of a simplex optimization method [20, 21] first that gives initial values for the Markov Chain Monte Carlo (MCMC) algorithm [22, 23, 24] also known as the Metropolis-Hastings method. Indeed, the MCMC allows accounting with the uncertainty on the known parameters (layer thickness, thermal properties of known layers and some experimental parameters) within the identification process of the unknown (thermal conductivity of the layer of interest, cut-off frequency of the detector, thermal resistances at the interfaces between layers). However, since the MCMC technique requires making the simulation of the model a large number of time, it is therefore used the simplex method first in order to limit the time for the convergence at its minimum with the MCMC. In section 5, the proposed methodology is applied to identify the thermal conductivity of a amorphous GeTe layer, with submicrometric thickness, deposited on a silicon wafer.

Benefits of this front face periodic pulse photothermal radiometry (FF-PPTR) method are numerous since it offers an interesting alternative to the use of the thermoreflectance in the VIS or the modulation technique within the IR with respect to the sensitivity, the implementation and the cost. Application of the method to bulk materials is straightforward but it will have obviously more interest for thin films deposited on a substrate where accuracy of the temperature change measurements at the small times is of first importance. Indeed, the proposed approach allows increasing greatly the accuracy of the measurement at the small times without degrading the measurement quality at long times. This makes the method reliable to reconstruct the thermal behavior along decades of time. As described previously, the linearity requirement, for both the heat transfer within the investigated material as well as the relationship between the emitted radiation and the surface temperature, is ensured since the averaging enhances greatly the signal-noise ratio, which leads finally to significantly decrease the standard deviation of the identified thermal

properties.

2. Experimental setup

The experimental setup has been originally designed within the rear face configuration [25] and has been implemented within the front face one for this study as represented schematically in the figure 1. It is composed of a Coherent Matrix Q-switch Nd:YAG diode-pumped laser (1064 nm wavelength) delivering pulses in a continuous mode with repetition frequency $f_p = 1/T_r$. As shown from photodiode measurement reported in Fig. 2(a), it is assumed that the pulse is varying with time as a Gaussian function as:

$$M(t) = \exp\left(-(t - t_c)^2 / 2\,\sigma_p^2\right) \tag{1}$$

with σ_p is some nanoseconds and $t_c \sim 4\,\sigma_p$. The maximum pulse repetition frequency is $f_p = 100\,\text{kHz}$ and the maximum rms power (10 W) is reached with $f_p = 30\,\text{kHz}$. The distance between the sample and the laser being about 0.8 m, the laser beam radius at the surface of the sample is then close to $r_0 = 3.5$ mm ($< 3\,\text{mrad}$ divergence). A fast photodiode with 1 nsec rise time (Thorlabs DET 10A/M) is used to trigger the acquisition device that is a Picoscope 9000 (16 bit, $50\,\Omega$ input impedance). Two off-axis parabolic mirrors are implemented in order to collect the emitted radiation at the surface heated by the laser. A fast IR photovoltaic detector (Kolmar KMPV11), that is an integrated high frequency HgCdTe infrared detector/amplifier sensor covering wavelengths from 2 µm up to 12 µm, is used in order to monitor the temperature change at the heated surface, i.e., the front face. The HgCdTe detector is coupled to an internal DC with f_{cA} =20 MHz bandwidth transimpedance amplifier. Therefore, the cut-off frequency for the detector-amplifier system is as $f_c < f_{cA}$ but is not provided by the manufacturer. The edge of the square photovoltaic sensitive element is $A_d = 1\,\text{mm}$ and rise time τ_d is estimated to be about 25 nsec. The IR detector window is Ge anti-reflection coated to reject laser diffuse reflection from the heated surface. The sample and the detector are put at the focal point for both mirrors leading to make the image of the detector at the surface of the sample. Therefore, assuming the surface viewed by the detector is a disk with radius r_m, the measurement area is close to the area of the detector so that $\pi\, r_m^2 = A_d^2$.

The energy delivered by each pulse as well as the emissivity of the surface are unknown. It is therefore a very difficult task to reach the absolute heat flux delivered by the laser pulse as well as the absolute temperature change viewed by the detector at the heated surface. However, within the deposit-substrate configuration, the reference can be done easily given that the thermal properties of the substrate are well known. In that case, the signal can be normalized with respect to its maximum value. In addition, optical-to-thermal transducer thin film can be also deposited on the layer that will be characterized. In that case the transducer will play also the role of a reference for the measured signal. In both presented configurations, there is no need to measure the absolute heat flux and temperature change.

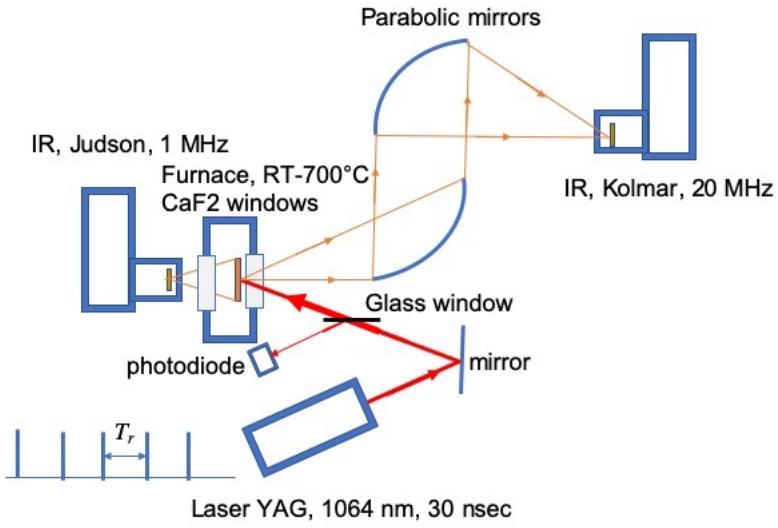

Figure 1: Experimental setup of the front face photothermal radiometry experiment where the laser pulse excitation is a N_s-pulse train periodically repeated with frequency $f_p = 1/T_r$.

Parameters t_c and σ_p in relation (1) have to be identified from experimental data provided by the photodiode. This is done using a minimization algorithm, the Nelder-Mead simplex method in the present case [20], that minimizes the quadratic gap between experimental values of $M(t)$ and calculated values from previous theoretical expression. An illustration is given in figure 2(a) where it is found $\sigma_p = 34$ nsec. In addition, this procedure allows also to find accurately the initial time of the experiment as presented in figure 2(b).

3. Mathematical model

3.1. Impulse response formulation

The derivation of the impulse response $\overline{h}(t)$ averaged over the disk with radius r_m aimed by the IR detector is classical within the field of thermal characterization and the results presented in the following are given without the need for a demonstration, which will be found in the literature [18, 17]. To summarize, the impulse response is expressed as:

$$\overline{h}(t) = \mathcal{L}^{-1}\left(\overline{H}(p)\right) = \int_{c-i\infty}^{c+i\infty} \overline{H}(p)\, \exp(-p\,t)\, \mathrm{d}p \tag{2}$$

Where $\mathcal{L}^{-1}$ denotes the inverse Laplace transform of the transfer function $\overline{H}(p)$. Given to the 2D-axi-symmetric experimental configuration, it is shown that:

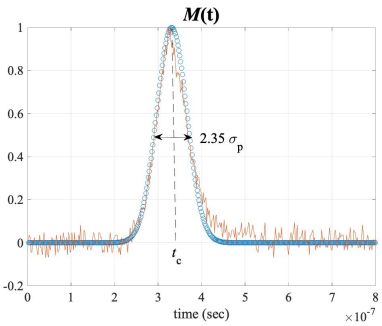

(a)

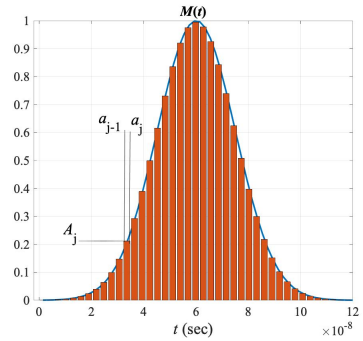

(b)

Figure 2: (a) parameters t_c and σ_p in relation (1) are identified from experimental values of $M(t)$ (red line). Calculated values of $M(t)$ from identified parameters are denoted by blue circles. (b) time 0 of the experiment is identified and the function $M(t)$ is approximated by linear piecewise functions that lead to easily calculate the Laplace transform $\Pi(p)$ of $M(t)$.

$$\overline{H}(p) = \frac{2}{r_m^2} \int_0^{r_m} r \int_0^{\infty} Z(\alpha, p)\; J_0(\alpha r)\; \psi(\alpha)\; \mathrm{d}\alpha\, \mathrm{d}r \tag{3}$$

In this relation $J_0()$ denotes the 0^{th} order Bessel function and $\psi(\alpha) = r_0^2 \exp\left(-\alpha^2 r_0^2/8\right)/4$ denotes the Hankel transform of the Gaussian function that is related to the spatial distribution of the laser beam as: $\exp\left(-r^2/2\,r_0^2\right)$. Considering a sample constituted from N_c layers with radius R_s, $(a_i,\, k_i,\, e_i)_{i=1,N_c}$ being the thermal diffusivity, the thermal conductivity and the thickness of each layer respectively, the function $Z(\alpha, p)$ is as:

$$Z(\alpha, p) = \frac{A + W_i\, B}{C + W_i\, D + W_s\,(A + H_i\, B)} \tag{4}$$

With W_i and W_s denoting the exchange coefficients at the rear and front faces respectively. Parameters A, B, C and D are calculated using the quadrupoles formalism[18] as:

$$\begin{bmatrix} A & B \\ C & D \end{bmatrix} = \begin{bmatrix} 1 & R_{T,1} \\ 0 & 1 \end{bmatrix} \begin{bmatrix} A_1 & B_1 \\ C_1 & D_1 \end{bmatrix} \prod_{j=2}^{N_c} \begin{bmatrix} 1 & R_{T,j} \\ 0 & 1 \end{bmatrix} \begin{bmatrix} A_j & B_j \\ C_j & D_j \end{bmatrix} \begin{bmatrix} 1 & R_{T,N_c+1} \\ 0 & 1 \end{bmatrix} \tag{5}$$

Where:

$$A_j = 1 + \exp(-2\,\gamma_i\, e_i)\,;\; B_j = (1 + \exp(-2\,\gamma_i\, e_i))\,/\gamma_i/k_i; \tag{6}$$

$$C_j = (1 + \exp(-2\,\gamma_i\, e_i))\;\gamma_i\, k_i;\; D_j = A_j \tag{7}$$

With $\gamma_i = \sqrt{p/a_i + \alpha^2}$. The variable $R_{T,j}$ $(2 \le j \le N_c)$ in (5) denotes the thermal resistance at the interface between layer $j-1$ and layer j whereas $R_{T,1}$ and R_{T,N_c+1} are thermal resistances that can simulate the presence of very thin

films at the front and rear surfaces respectively. The value for $\overline{H}(p)$ within relation (3) can be calculated using the Fourier-Bessel series for the integral (3) as:

$$\overline{H}(p) = \frac{r_0^2}{2\,R_s^2}\,Z(\alpha_0, p) + \sum_{n=1}^{\infty} \frac{J_1(\alpha_n\,r_m)\;r_0^2\,e^{-\frac{\alpha_n^2\,r_0^2}{8}}}{r_{\mathrm{m}}\,\alpha_n\,R_s^2\,J_0(\alpha_n\,R_s)^2}\,Z(\alpha_n, p) \tag{8}$$

where R_s denotes the sample radius and $J_1()$ denotes the 1^{th} order Bessel function. The values for α_n are the roots of the boundary conditions at $r = R_s$. Assuming that the circumference is insulated, those values are as:

$$\alpha_n\,R_s \approx \pi\left(n + \frac{1}{4}\right) - \frac{3}{8\,\pi\left(n+\frac{1}{4}\right)},\ \alpha_0 = 0 \tag{9}$$

Considering a thin film (d), with thickness e_d, deposited on a substrate (s), the relation (8) can be simplified when the Fourier number related to the deposit is such as $Fo \ll r_0^2/4\,e_d^2$, if $e_d \gg r_0$ and $t \ll r_0^2/4\,a_s$ otherwise. Indeed, in such a case, the heat transfer becomes one-dimensional and the second term of the sum in relation (8) vanishes leading to $\overline{H}(p) \sim Z(\alpha_0, p) = Z(p)$ with $\alpha_0 = 0$. It is obviously recommended to adapt the experimental parameters to work within the 1D configuration since it avoids uncertainty on both r_0 and r_m. On the other hand, the heat loss at the front face can be neglected for the duration of the experiment and also because the oven of the furnace is filled by Argon in order to prevent oxidation. In addition, the rear face of the sample is fixed at the temperature of the furnace. Assuming the 1D working condition is fulfilled, all of this finally comes to simplify relation (4) as: $\overline{H}(p) = Z(p) = B/D$.

3.2. Temperature change for one pulse

As said previously, the function $M(t)$ that describes the time-varying pulse waveform is given by relation (1). Let us note $\Pi(p) = \mathcal{L}(M(t))$ the Laplace transform of $M(t)$. In addition, in order to account with the cut-off frequency of the detector f_c and delay τ_d, the transfer function of the detector is considered as a delayed first-order low-pass filter as:

$$D(p) = \exp(-\tau_d\,p)\,/\,(1 + p/2\pi f_c) \tag{10}$$

It can be thus expressed the average relative temperature change viewed by the detector considering one pulse as:

$$\overline{\triangle T_u}(t) = \mathcal{L}^{-1}\left(\overline{\triangle\theta_u}(p)\right) \tag{11}$$

With:

$$\overline{\triangle\theta_u}(p) = \overline{H}(p)\;\Pi(p)\;D(p) \tag{12}$$

Where $\overline{H}(p)$ has been derived in the previous section.

3.3. Response to the periodic pulse waveform

Let us consider now that the heat flux is generated as a sequence of pulses with repetition frequency $1/T_r$. Therefore the excitation is described as a convolution production between the time-varying pulse waveform $M(t)$ and the Dirac comb $I_p(t)$ as:

$$I_p(t) = \sum_{n=-\infty}^{+\infty} \delta(t - n\,T_r) \tag{13}$$

Therefore, the average temperature $\overline{T}(t)$ at the area aimed by the detector at the front face of the sample is given from the convolution product between the response $\overline{\triangle T_u}(t)$, relation (11), and the periodic pulse sequence. Using relation (13) and the associating property of the convolution product, this leads to:

$$\overline{\triangle T}(t) = \overline{\triangle T_u}(t) * I_p(t) = \overline{\triangle T_u}(t) * \left[\sum_{n=-\infty}^{+\infty} \delta(t - n\,T_r)\right] \tag{14}$$

Expressing the convolution product leads to:

$$\overline{\triangle T}(t) = \int_{-\infty}^{\infty} \overline{\triangle T_u}(t-\tau) \sum_{n=-\infty}^{+\infty} \delta(\tau - n\,T_r)\,\mathrm{d}\tau \tag{15}$$

That is also:

$$\overline{\triangle T}(t) = \sum_{n=-\infty}^{+\infty} \int_{-\infty}^{\infty} \overline{\triangle T_u}(t-\tau)\,\delta(\tau - n\,T_r)\,\mathrm{d}\tau = \sum_{n=-\infty}^{+\infty} \overline{\triangle T_u}(t + nT_r) \tag{16}$$

Due to the nature of the impulse response ($\overline{\triangle T_u} = 0$ for $t < 0$) et since the upper limit of the series can be bounded to M value in practice, the relation (16) is calculated as:

$$\overline{\triangle T}(t) = \sum_{0}^{M} \overline{\triangle T_u}(t + nT_r), \text{ for } 0 \le t \le T_r \tag{17}$$

Obviously, it can be also calculated the average temperature $\overline{\triangle T_n}(t)$ for each pulse n $(0 \le n \le M)$ as:

$$\overline{\triangle T_n}(t) = \overline{\triangle T_{n-1}}(t) + \overline{\triangle T_u}(t + nT_r), \text{ for } (n-1)\,T_r \le t \le n\,T_r, \text{ with } \overline{\triangle T_{-1}}(t) = 0 \tag{18}$$

3.4. Numerical aspects

The Laplace transform of function $M(t)$, defined by relation (1), is $\Pi(p) = A\sqrt{\pi}\,\sigma_p \exp\left(p^2\,\sigma_p^2\right) \operatorname{erfc}(p\,\sigma_p) \exp(-p\,t_c)$, where erfc() is the complementary error function with complex argument. In such a case the erfc() function does not converge easily when $p \to \infty$, i.e., when $t \to 0$, and it is better approaching the function $M(t)$ with constant piecewise functions as represented in figure 2(b). In that case, the Laplace transform of this function is simply:

$$\Pi(p) = A_j \sum_j \left(\exp(-a_{j-1}p) - \exp(-a_j p)\right)/p \tag{19}$$

where a_{j-1} and a_j denote the time interval for the j^{th} linear segment and A_j is the corresponding amplitude as showed on the figure.

The computation of $\overline{\triangle\theta_u}(p)$ starts by calculating (i) $\overline{H}(p)$ from relation (8), (ii) $\Pi(p)$ from relation (19) and (iii) $D(p)$ from relation (10). Then, $\overline{\triangle\theta_u}(p)$ is calculated from relation (12). The inverse Laplace transform of $\overline{\triangle\theta_u}(p)$, which leads to $\overline{\triangle T_u}(t)$, is calculated using the de Hoog algorithm[26, 27, 28] that is a fast and accurate method based on a Gaussian quadrature rule and a Padé-type accelerator to approximate the series under the form of a continued fraction whose numerators and denominators are defined by recurrence. Finally the quantity $\overline{\triangle T}(t)$ that is proportional to the temperature change at the area aimed by the IR detector, is calculated using relation (17). Since the amplitude of the pulse energy is unknown, we will introduce the relative change of temperature, with respect to its maximum value as:

$$\overline{\triangle T_{norm}}(t) = \frac{\overline{\triangle T}(t)}{\max\left[\overline{\triangle T}(t)\right]} \tag{20}$$

The value of M in relation (17) has to be chosen so that the series converges, meaning the time-varying temperature calculated at M is not significantly different from that calculated with $(M-1)$ whatever the time t. Let us consider a material, with $k = 10$ W/m/K, $\rho = 6140$ (kg/m^3), $C_p = 190$ (J/kg/K) and thickness $e = 0.1$ mm. The repetition frequency of the pulse is $f_p = 1/T_r = 0.2$ MHz, the duration of the pulse is 50 ns, the rise time and cut-off frequency of the detector are respectively 20 ns and 10 MHz. The temperature for each pulse n, with $0 \leq n \leq M = 500$ is calculated from relation (18) and plotted in figure 3(a). The continuous regime is well indicated on the plot and a constant value is reached starting from $M = 320$. This indicates thus clearly the time from which the time averaging process of the experimental response can be performed. This averaging will lead to significantly increase the signal noise ratio as said in the introduction. The figure 3(b) shows the impulse response calculated for $n = 0$, $n = 50$ and $n = 500$ on the repetition period time range $(0,\ T_r)$ within a logarithm scale for both axis. The slope -1/2, which is a feature of the semi-infinite behavior with $n = 0$ at the small times, is lost when approaching the value of T_r since the impulse response vanishes in order to retrieve the value at $t = 0$. This highlights well the choice of M in order to mimic the experimental response. Decreasing the value of k or increasing the value of f_p will lead to increase the

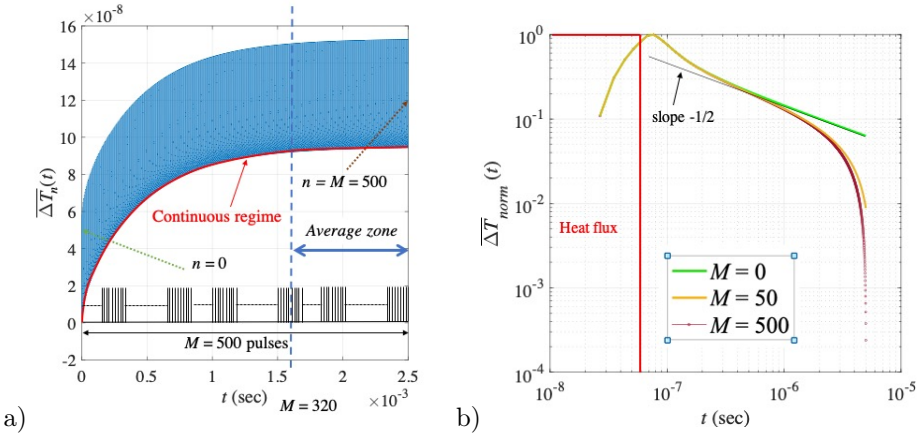

Figure 3: (a) calculated temperature change considering the Dirac comb from relation (18) and (b) calculated normalized temperature change for different value of M.

	k (W/m/K)	ρ(kg/m^3)	C_p (J/kg/K)	e (m)
deposit	30-3-0.3	6140	190	$[100-400]\times10^{-9}$
substrate	148	2300	700	0.6×10^{-3}

Table 1: Thermophysical properties of the deposit and the substrate used for the sensitivity analysis.

value of M. In practice, since the computation time for relation (17) is very low (less that the second, proc i7, 3.1 GHz), the choice of Mwill be made by successive trials until the calculation with M will not differ significantly from that calculated with $(M-1)$ whatever the time t.

4. Sensitivity analysis and Identification procedure

Let us consider a deposit-on-substrate configuration where thermal properties are reported in Tab. 1 and assuming a thermal resistance R_T at the interface between the deposit and the substrate.

The dimensionless sensitivity functions for both the deposit thermal conductivity k_d and the thermal resistance R_T at the deposit-substrate interface are calculated using a difference scheme as:

$$S_\alpha^T(t) = \alpha\frac{\mathrm{d}\triangle T_r(t)}{\mathrm{d}\alpha} = \frac{\triangle T_r(t)_{\alpha+0.1\alpha} - \triangle T_r(t)_\alpha}{0.1},\ \alpha \equiv \{k_d, R_T\} \tag{21}$$

The two sensitivity functions are calculated and reported in figure 4(a), (b) and (c) considering respectively three different values for the deposit thermal conductivity k_d, namely 30, 3 and 0.3 W/m.K. The repetition frequency is $f_p = 0.1$ MHz, the value of M is 100 and the deposit thickness is $e_d = 400$

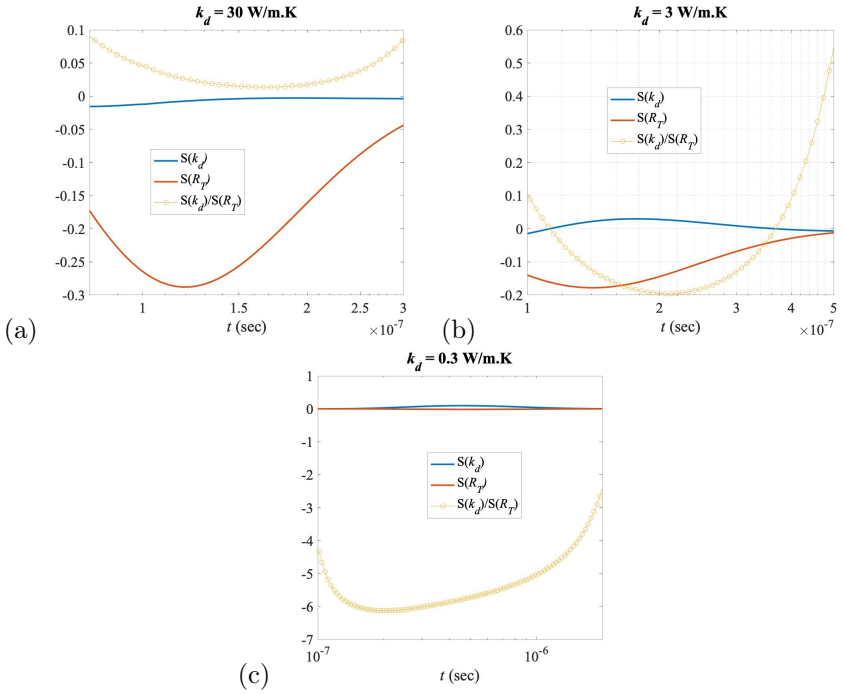

Figure 4: Sensitivity functions of the calculated relative temperature change from relation (20) to the thermal conductivity k_d of the deposit and to the thermal resistance R_T at the deposit-substrate interface. The sensitivity for parameter α is calculated as: $S_\alpha^T(t) = \alpha\, \mathrm{d}\triangle T_r(t)/\mathrm{d}\alpha$. The ratio for the two sensitivity functions allows checking the linear dependence of the functions. Three values of the deposit thermal conductivity are considered showing its influence on the linear dependence of both sensitivity functions.

nm. The ratio of the two sensitivity functions is also reported in the same figures. The thermal conductivity of the substrate k_s being high the figures show that both sensitivity functions are linearly independent if the thermal conductivity of the deposit if high. Indeed, the highest the value of k_d, the highest the sensitivity on R_T. This result is well-known and is not dependent on the value of M. If this condition is satisfied, it allows identifying both parameters within a minimization operation of the gap between the calculated time-varying temperature and that obtained from an experiment.

The value of the detector cut-off frequency is also of first importance since it has a strong influence on the measured signal as presented in the figure 5. The identification of k_d, f_c and R_T using experimental values of the signal at the IR detector, normalized with respect to its averaged maximum value, is based first on the Nelder-Mead Simplex (NMS) method. This technique allows finding very rapidly the values of those parameters that allows minimizing the criterion $J = \sum_{n=1}^{N} \left(y(t) - \triangle T_r(t)\right)^2$ where $y(t)$ denote the experimental values and $\triangle T_r(t)$ are the ones calculated from the model, i.e., relation (20). However, this technique does not account on the uncertainty on known parameters as

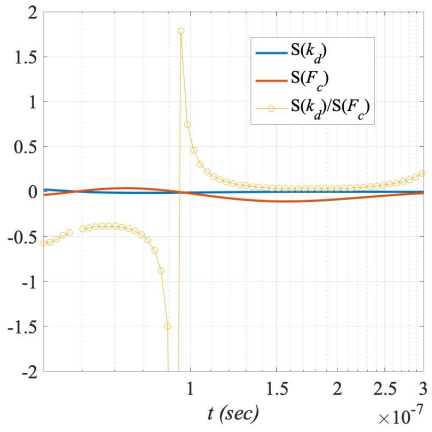

Figure 5: Sensitivity function of the calculated relative temperature change from relation (20) to the thermal conductivity k_d of the deposit and to the detector cut-off frequency f_c.

the layer thicknesses for example. Therefore, the Markov Chains Monte Carlo method (MCMC) also known as the Metropolis algorithm has been implemented using the identified values of the parameters as those found using the NMS.

5. Illustration

In order to highlight the advantages of the proposed technique, we considered amorphous GeTe (a-GeTe) film deposited by magnetron sputtering in an Ar atmosphere on a Si substrate capped with 500 nm SiO_2 thermal oxide at the top. The GeTe film is capped with a Pt film, 100 nm thick, that plays the role of the optical-to-thermal transducer and that also makes the absorption of the laser at the surface since GeTe is not opaque at the laser wavelength. All the thermophysical properties of those material are reported in table 2. The thermal conductivity of amorphous GeTe was found equal to 0.22 ± 0.02 W/(m.K) using the modulated photothermal radiometry (MPTR) technique that allows measuring the thermal resistance of the stack of layers (Pt/GeTe/SiO_2) deposited on the Si substrate [29]. The GeTe has been deposited at four different thicknesses, e.g., (100, 200, 300, 400) nm. In addition, the MPTR leads to the total thermal resistance at the Pt-GeTe and GeTe-SiO_2 interfaces as; $R_{Pt-GeTe} + R_{GeTe-SiO_2} = (22.6 \pm 7.2) \times 10^{-8}\,\mathrm{m}^2.\mathrm{K/W}$. This value seems quite high but it must be said that the mechanical/chemical adhesion between Pt and GeTe is very low [30]. Those data will serve as references in order to check the accuracy of the FF-PPTR.

The $N_s = 4000$ averaged measured signal at the IR detector is normalized with respect to its average maximum and reported in figure 6 for the four thicknesses values of the GeTe layer. Since a low thermal conductivity of the a-GeTe is expected, the previous sensitivity analysis leads us to identity the thermal

Table 2: Thermophysical properties of the layers deposited on the Si substrate. Thermal conductivity, density and specific heat of Pt and SiO_2 are found in [31]. The specific heat and density of a-GeTe are given in [32] and [33] respectively. Thermal conductivity of a-GeTe measured using the MPTR is reported in [29] and data from literature are also available [34].

	k (W/m/K)	ρ(kg/m^3)	C_p (J/kg/K)	e (m)
transducer (Pt)	72	21350	130	$[100 \pm 10] \times 10^{-9}$
deposit (GeTe)	0.22 ± 0.02[29]	6140[33]	190[32]	$[100 - 400] \pm 10 \times 10^{-9}$
substrate (SiO_2)	1.45	4500	540	500×10^{-9}
substrate (Si)	148	2300	700	0.6×10^{-3}

conductivity k_{GeTe} of the a-GeTe film and the detector cut-off frequency f_c . Indeed, following the resulys of the sensitivity analysis, the thermal resistances $R_{Pt-GeTe}$ at the Pt-GeTe interface and $R_{GeTe-SiO_2}$ at the GeTe-SiO2 one cannot be identified separately from k_{GeTe}. As a first step it is assumed the following values for the resistances: $R_{Pt-GeTe} = 2 \times 10^{-7}$ K.m^2/W and $R_{GeTe-SiO_2} = 3 \times 10^{-8}$ K.m^2/W. The initial values for k_{GeTe} and f_c are 0.05 W/m/K and 10 MHz respectively. Using the Nelder-Mead Simplex (NMS) method, it was found the optimal values for both parameters, see table 3. For all those calculations the value of $M = 100$ was chosen in relation (17).

Discrepancies between the value of k_{GeTe} for the four values of the a-GeTe film thickness is small apart for the value for the lowest thickness. Indeed, as presented in figure 6(b), the Fourier number associated to the GeTe layer, $Fo = a_{GeTe}\, t/e^2_{GeTe}$, is very large whatever the time value. It means obviously that the data do not bring information about the diffusion within the GeTe layer. Regarding the other three thicknesses the identified value for k_{GeTe} is close to the measured value using the MPTR.

Using the MCMC method, large standard deviation has been introduced on $R_{Pt-GeTe}$ ($\left[10^{-7} - 5 \times 10^{-7}\right]$ K.m^2/W) and $R_{GeTe-SiO_2}$ ($\left[10^{-8} - 10^{-7}\right]$ K.m^2/W) but also on e_{GeTe} and e_{Pt} since those parameters may slightly vary from expectations to real configuration (10 nm for the two layers). The identified mean value for those parameters have been reported in table 3 and the average temperature at the front face is calculated using those identified values and reported in figure 6(a) for the four thicknesses of the a-GeTe layer. It is found a very nice agreement between the measurements and the calculated values using the identified parameters. Regarding the calculated standard deviation, the identified mean value for k_{GeTe} is also very close to the value measured using the MPTR. The cut-off frequency of the detector is found almost constant at 8.5 MHz, which is coherent since it does not depend on the GeTe layer thickness. The mean thickness for the GeTe and Pt layers are strictly equal to that prescribed for the deposition process. As expected, the uncertainty on the thermal resistance at the two interfaces of the GeTe layer is high. The Geweke param-

Table 3: Identified values for k_{GeTe} and f_c using first the Nelder-Mead Simplex (NMS) method. Those values are used as the initial ones for the Markov Chains Monte Carlo (MCMC) method that leads to estimated mean values for k_{GeTe}, $R_{Pt-GeTe}$, $R_{GeTe-SiO_2}$, F_c, e_{GeTe} and e_{Pt}. The standard deviation for the parameters is reported according to their prior distribution. The Geweke parameter [35] value for the states convergence has been reported for all the variables involves within the MCMC minimization process.

e_{GeTe} (nm)	Minimization technique	k_{GeTe} (W/m/K), G	$R_{Pt-GeTe}$ (K.m^2/W), G $R_{GeTe-SiO_2}$ (K.m^2/W), G F_c (MHz), G e_{GeTe} (nm), G e_{Pt} (nm), G
100	NMS	0.318	– – 6.13 – –
	MCMC	0.654 ± 0.20, 0.80	$[3.54 \pm 0.97] \times 10^{-7}$ 0.88 $[5.86 \pm 2.48] \times 10^{-8}$ 0.24 8.3 ± 2.81 , 0.93 100 ± 5 0.99 100 ± 5 0.99
200	NMS	0.230	– – 7.12 – –
	MCMC	0.267 ± 0.04, 0.94	$[2.75 \pm 1.05] \times 10^{-7}$ 0.79 $[7.22 \pm 2.25] \times 10^{-8}$ 0.60 8.56 ± 2.76 , 0.95 200 ± 5 0.99 100 ± 5 0.99
300	NMS	0.232	– – 8.48 – –
	MCMC	0.25 ± 0.25, 0.90	$[3.01 \pm 1.12] \times 10^{-7}$ 0.53 $[5.36 \pm 2.56] \times 10^{-8}$ 0.53 9.41 ± 3.1 , 0.97 300 ± 5 0.99 100 ± 5 0.99
400	NMS	0.248	– – 7.93 – –
	MCMC	0.27 ± 0.04, 0.96	$[2.72 \pm 1.14] \times 10^{-7}$ 0.42 $[6.01 \pm 2.6] \times 10^{-8}$ 0.26 8.49 ± 2 , 0.92 400 ± 5 0.99 100 ± 5 0.99

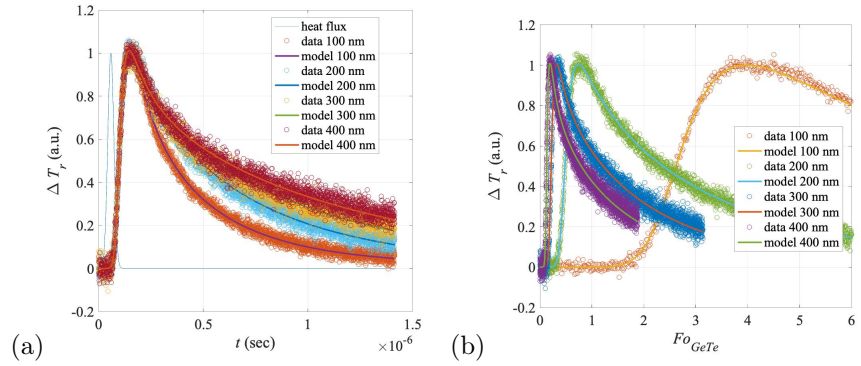

Figure 6: (a) experimental values of the signal of the IR detector averaged 4000 times and normalized relatively to the average maximum value (empty circles) and calculated average relative temperature change at the area aimed by the detector using the model (plain line, relation (20)) according to the time t. (b) experimental and theoretical values are plotted according the Fourier number of the deposit $Fo = a_{GeTe}\, t/e^2_{GeTe}$ where a_{GeTe} and e_{GeTe} denote the thermal diffusivity and the thickness of the a-GeTe layer.

eter G, that measures the convergence of the states for each parameter during the MCMC process, has been reported in table 3. It is close to 1 for k_{GeTe}, F_c, e_{Pt} and e_{GeTe} but rather far from this value for $R_{Pt-GeTe}$ and $R_{GeTe-SiO_2}$. This is well consistent of course with the calculated standard deviation and the sensitivity analysis. An example of results achieved using the MCMC technique has been reported in figure 7 considering the thickness $e_{GeTe} = 300$ nm of the a-GeTe layer. The method allows calculating the 50%, 90%, 95% and 99% confidence interval on the temperature $\triangle T_r$, see 7(a), using the mean value $\overline{p}$ of the histogram represented in figure7(b) for each parameter. As predicted, if a priori densities and measurement noise are Gaussian, a posteriori densities $\mathcal{N}(\overline{p}, \sigma_p)$ are Gaussian as well for parameter p. This is well retrieved by the MCMC algorithm for parameters $p \equiv (k_{GeTe}, F_c, e_{GeTe}, e_{Pt})$. For parameters $(e_{GeTe}; e_{Pt})$, the Gaussian shape is not so clear due to the search interval specified in the algorithm. The mean values are visible nonetheless. Concerning $R_{Pt-GeTe}$ and $R_{GeTe-SiO2}$, this experimental setup does not provide enough information to obtain reliable mean values. Standard deviation is indeed too large. However, it is still possible to consider the thermal resistance of the GeTe layer, defined as $R_T = R_{Pt-GeTe} + e_{GeTe}/k_{GeTe} + R_{GeTe-SiO_2}$, as a function of the GeTe layer thickness e_{GeTe}. The plot is represented in figure 8. The calculated linear regression shows that the sum of the two resistances at the interfaces is such as: $R_{Pt-GeTe} + R_{GeTe-SiO_2} = 2.1 \times 10 - 7\,\mathrm{K.m^2/W}$ and that the mean thermal conductivity of the GeTe layer is $k_{GeTe} = 1/4.2 = 0.238\,\mathrm{W/(m.K)}$. Those values are very close to that found using the MPTR.

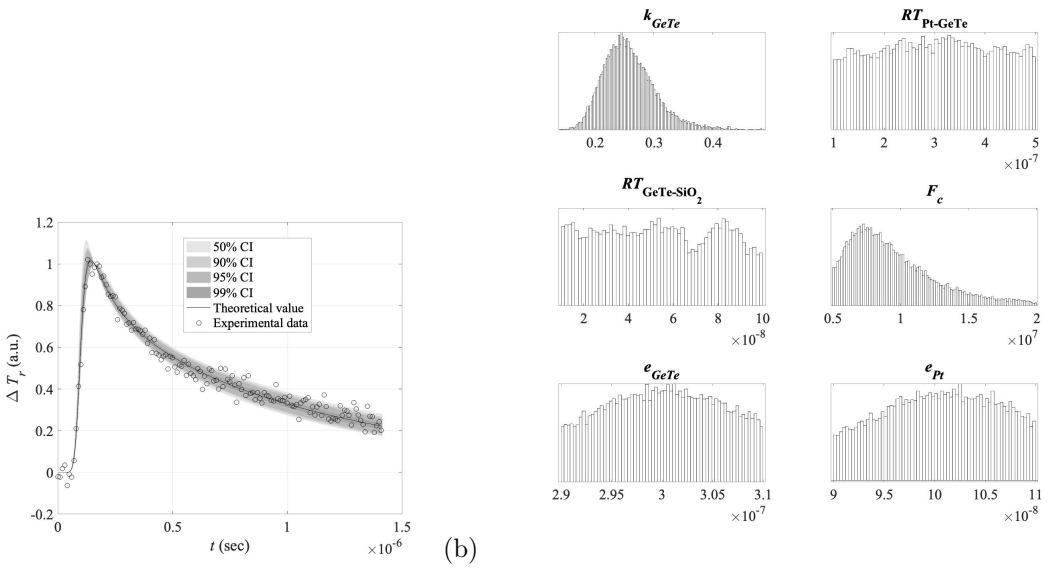

Figure 7: (a) comparison between experimental data and theoretical calculus for $\triangle T$ considering the a-GeTe layer with 300 nm thickness. The 50%, 90%, 95% and 99% confidence intervals have been also reported. (b) histogram of the states for the parameters involved within the MCMC minimization.

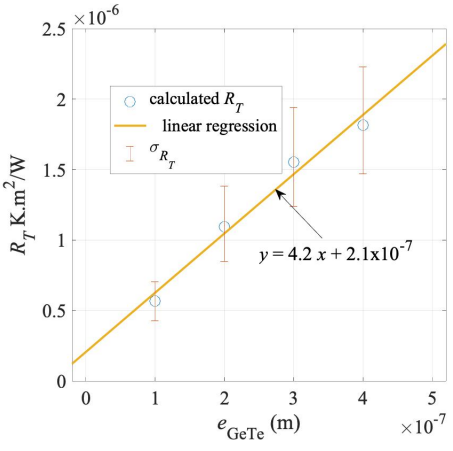

Figure 8: Calculated R_T from identified mean values reported in table 3 and associated standard deviation. The coefficient of determination is $R^2 = 0.96$.

6. Conclusion

The front face periodic pulse photothermal radiometry (FF-PPTR) technique has been presented in this study. Averaging the measured signal between two successive pulses a large number of times, starting when the continuous regime is reached, leads obviously to increase very significantly the signal noise ratio. It is therefore obtained an exploitable signal that is involved within a minimization procedure in order to identify the seek parameters. The repetition frequency of the pulse is considered within the derivation of the theoretical response as well as the measured relative heat flux as a function of time. The IR detector features (cut-off frequency and delay) have been also considered as a delayed first-order low pass filter. A simplex minimization algorithm has been used to give initial starting point for a MCMC algorithm that involves uncertainties on known experimental parameters. An illustration of the proposed technique has been given that consists in identifying the thermal conductivity of an amorphous GeTe thin film deposited on a Si substrate. This configuration having being treated using the modulated photothermal radiometry technique (MPTR), a comparison has been made with the results obtained using the proposed FF-PPTR technique. It was found a very good agreement between the results from the two experimental techniques. The FF-PPTR appears thus as a significant improvement of the classical flash method, in terms of reliability and accuracy and an alternative to the thermoreflectance and the modulated photothermal radiometry for high frequency. The proposed optimization methodology allows also to compute the uncertainty on the identified values by accounting with the uncertainty on the known experimental parameters. Finally, this approach allows implementing even faster IR detectors with the potential to explore nanoseconds time range and thus to investigate heat diffusion within layers of very small thickness.

References

[1] D. G. Cahill, Thermal conductivity measurement from 30 to 750 k: the 3ω method, Review of Scientific Instruments 61 (2) (1990) 802–808.

[2] C. E. Raudzis, F. Schatz, D. Wharam, Extending the 3ω method for thin-film analysis to high frequencies method for thin-film analysis to high frequencies, Journal of Applied Physics 93 (10) (2003) 6050–6055.

[3] D. G. Cahill, Analysis of heat flow in layered structures for time-domain thermoreflectance, Review of Scientific Instruments 75 (12) (2004) 5119–5122.

[4] T. Baba, K. Ishikawa, T. Yagi, N. Taketoshi, Measurements of Thermophysical Property of Thin Films by Light Pulse Heating Thermoreflectance Methods, arXiv e-prints (Sep 2007).

[5] M. G. Burzo, P. L. Komarov, P. E. Raad, Optimized thermo-reflectance system for measuring the thermal properties of thin-films and their interfaces, in: Twenty-Second Annual IEEE Semiconductor Thermal Measurement And Management Symposium, 2006, pp. 87–94.

[6] W. S. Capinski, H. J. Maris, Improved apparatus for picosecond pump and probe optical measurements, Review of Scientific Instruments 67 (8) (1996) 2720–2726.

[7] N. Taketoshi, T. Baba, E. Schaub, A. Ono, Homodyne detection technique using spontaneously generated reference signal in picosecond thermoreflectance measurements, Review of Scientific Instruments 74 (12) (2003) 5226–5230.

[8] S. Dilhaire, G. Pernot, G. Calbris, J. M. Rampnoux, S. Grauby, Heterodyne picosecond thermoreflectance applied to nanoscale thermal metrology, Journal of Applied Physics 110 (11) (2011) 114314.

[9] M. Depriester, P. Hus, S. Delenclos, A. H. Sahraoui, New methodology for thermal parameter measurements in solids using photothermal radiometry, Review of Scientific Instruments 76 (7) (2005) 074902.

[10] A. Salazar, A. Oleaga, A. Mendioroz, E. Apiñaniz, Thermal effusivity measurements of thermal insulators using the photopyroelectric technique in the front configuration, Measurement 121 (2018) 96 – 102.

[11] P.-E. Nordal, S. O. Kanstad, Photothermal radiometry, Physica Scripta 20 (5-6) (1979) 659–662.

[12] S. André, B. Rémy, D. Maillet, A. Degiovanni, J.-J. Serra, Modulated photothermal radiometry applied to semitransparent samples: Models and experiments, Journal of Applied Physics 96 (5) (2004) 2566–2575.

[13] J.-L. Battaglia, A. Kusiak, M. Bamford, J.-C. Batsale, Photothermal radiometric characterization of a thin deposit using a linear swept-frequency heat flux waveform, International Journal of Thermal Sciences 45 (11) (2006) 1035 – 1044.

[14] N. Horny, M. Chirtoc, A. Fleming, G. Hamaoui, H. Ban, Kapitza thermal resistance studied by high-frequency photothermal radiometry, Applied Physics Letters 109 (3) (2016) 033103. arXiv:https://doi.org/10.1063/1.4959084, doi:10.1063/1.4959084.
URL `https://doi.org/10.1063/1.4959084`

[15] J. V. Beck, K. J. Arnold, Parameter estimation in engineering and science, wiley Edition, 1977.

[16] R. Aster, B. Borchers, C. H. Thurber, Parameter Estimation and Inverse Problems, Elsevier Science, 2018.

[17] C. H.S., J. J.C., Conduction of heat in solids, oxford: clarendon Edition, 1959.

[18] D. Maillet, S. André, J.-C. Batsale, A. Degiovanni, C. Moyne, Thermal quadrupoles : solving the heat equation through integral transforms, wiley Edition, 2000.

[19] A. Degiovanni, C. Pradere, E. Ruffio, J.-L. Battaglia, Advanced thermal impedance network for the heat diffusion with sources, International Journal of Thermal Sciences 130 (2018) 518 – 524.

[20] R. H. Byrd, J. C. Gilbert, J. Nocedal, A trust region method based on interior point techniques for nonlinear programming, Mathematical Programming 89 (1) (2000) 149–185.

[21] D. Wilde, C. Beightler, Foundations of Optimization, Prentice-Hall, 1967.

[22] W. K. Hastings, Monte carlo sampling methods using markov chains and their applications, Biometrika 57 (1) (1970) 97–109.

[23] J. P. Kaipio, C. Fox, The bayesian framework for inverse problems in heat transfer, Heat Transfer Engineering 32 (9) (2011) 718–753. arXiv:https://doi.org/10.1080/01457632.2011.525137, doi:10.1080/01457632.2011.525137.
URL https://doi.org/10.1080/01457632.2011.525137

[24] H. R. B. Orlande, G. S. Dulikravich, M. Neumayer, D. Watzenig, M. J. Colaço, Accelerated bayesian inference for the estimation of spatially varying heat flux in a heat conduction problem, Numerical Heat Transfer, Part A: Applications 65 (1) (2014) 1–25. arXiv:https://doi.org/10.1080/10407782.2013.812008, doi:10.1080/10407782.2013.812008.
URL https://doi.org/10.1080/10407782.2013.812008

[25] E. Ruffio, C. Pradere, A. Sommier, J.-C. Batsale, A. Kusiak, J.-L. Battaglia, Signal noise ratio improvement technique for bulk thermal diffusivity measurement, International Journal of Thermal Sciences 129 (2018) 385 – 395.

[26] F. R. de Hoog, J. H. Knight, A. N. Stokes, An improved method for numerical inversion of laplace transforms, SIAM Journal on Scientific and Statistical Computing 3 (3) (1982) 357–366.

[27] J. Abate, P. P. Valkó, Multi-precision laplace transform inversion, International Journal for Numerical Methods in Engineering 60 (5) (2004) 979–993.

[28] K. Boupha, J. M. Jacobs, K. Hatfield, Mdl groundwater software: Laplace transforms and the de hoog algorithm to solve contaminant transport equations, Computers and Geosciences 30 (5) (2004) 445 – 453.

[29] A. Kusiak, J.-L. Battaglia, P. Noé, V. Sousa, F. Fillot, Thermal conductivity of carbon doped GeTe thin films in amorphous and crystalline state measured by modulated photo thermal radiometry, in: Journal of Physics Conference Series, Vol. 745 of Journal of Physics Conference Series, 2016, p. 032104.

[30] J. Orava, T. Kohoutek, T. Wagner, 9 - deposition techniques for chalcogenide thin films, in: J.-L. Adam, X. Zhang (Eds.), Chalcogenide Glasses, Woodhead Publishing, 2014, pp. 265 – 309.

[31] W. Martienssen, H. Warlimont, Springer Handbook of Condensed Matter and Material Data, Springer Berlin Heidelberg, New York, 2005.

[32] Q. Xu, K. Ichikawa, Kinetic aspects of heat capacity in the annealing of ge20te80glasses, Journal of Physics C: Solid State Physics 19 (36) (1986) 7145–7156.

[33] T. Nonaka, G. Ohbayashi, Y. Toriumi, Y. Mori, H. Hashimoto, Crystal structure of gete and ge2sb2te5 meta-stable phase, Thin Solid Films 370 (1) (2000) 258 – 261.

[34] P. Nath, K. Chopra, Thermal conductivity of amorphous and crystalline ge and gete films, prb 10(8) (1974) 3412–3418.

[35] J. Geweke, Evaluating the accuracy of sampling-based approaches to the calculation of posterior moments, in: in Bayesian Statistics, University Press, 1992, pp. 169–193.